AAS 18-400

MULTI-SPHERE METHOD FOR FLEXIBLE CONDUCTING SPACE OBJECTS: MODELING AND EXPERIMENTS

Jordan Maxwell*, Kieran Wilson†, Mahdi Ghanei‡, and Hanspeter Schaub§

In the last two decades, concepts have been developed to harness electrostatic forces and torques to enable new categories of missions, from formation flying to inflating membrane structures or detumbling and reorbiting debris touchlessly. The need for faster-than-realtime modeling of the electrostatic forces and torques in these missions has led to the development of the Multi-Sphere Method (MSM) in which the electrostatic field generated by a charged body is approximated through the use of a series of optimally placed and sized conducting spheres. While the prior work assumed the charged body is rigid, this paper extends the use of MSM to flexible shapes. The effectiveness of the flexible MSM approach is shown using an analytical matching with a line deforming into a circle. However, the core underlying assumption of the shape surface being a conductor remains. To explore how well this flexible shape model allows for charge membrane deflections to be modeled, a thin aluminum coated mylar strip is exposed to a constant electric field in a vacuum chamber. The results indicated that with a given field and high strip potentials the deflections are modeled well. However, the experiments also illustrate that the dielectric mylar material causes significant dynamic response changes. While the flexible MSM approach is a good method to approximate the electrostatic forces and torques on a general shape, the limiting case of extremely thin mylar sheets illustrate that additional physical phenomena must be modeled to predict the motion of such objects.

INTRODUCTION

In the severely resource-constrained environment of space, the concept of low-mass and fuel-less electrostatic actuation has been considered an attractive proposition throughout the space age. Initial studies, originating with Reference [1] in 1966, investigated electrostatic inflation of reflective membrane structures as a mass effective alternative to traditional deployable antennas. Later investigation of electrostatic membrane inflation has shown these forces to be sufficient to maintain inflation under orbital perturbations, with the assistance of mechanical structures to achieve a desired shape.[2, 3] The use of mechanical constraints to shape the membrane eliminates the need to model the dynamics of the system, as experimental results demonstrated that the membrane will inflate satisfactorily given sufficient electrostatic pressure.

However, not all membranes subject to electrostatic inflation are constrained or designed to inflate in a predictable fashion. This is particularly relevant in the field of High Area-to-Mass Ration (HAMR) debris objects in high altitude orbits, especially in the geosynchronous region (GEO).

*Graduate Research Assistant, Aerospace Engineering Sciences, University of Colorado.
†Graduate Research Assistant, Aerospace Engineering Sciences, University of Colorado.
‡Undergraduate Research Assistant, Mechanical Engineering, University of Colorado.
§Glenn L. Murphy Endowed Chair, Associate Chair of Graduate Affairs, Department of Aerospace Engineering Sciences, University of Colorado, 431 UCB, Colorado Center for Astrodynamics Research, Boulder, CO 80309-0431. AAS Fellow

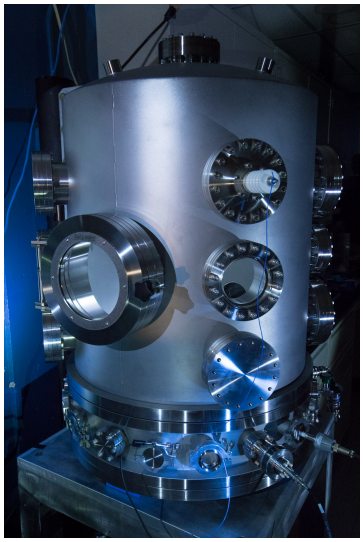

Figure 1. The ECLIPS space environment simulation testbed

The orbits of these objects are more influenced by electrostatic perturbations than other craft, and strongly subject to variations in solar radiation pressure resulting from attitude variation.[4] For the rigid flat plate considered by References [5] and [6], however, electrostatic forces are a far smaller influence on the orbit than attitude perturbations. Through the coupling with the solar radiation pressure they are shown to impact the orbital motion.[5, 7]

One category of HAMR debris object is likely to see much larger orbital effects because of electrostatic perturbations: flexible materials, such as pieces of aluminized mylar. As the mylar flexes and changes its shape, the resulting solar radiation pressure will change accordingly. In Reference [8] the perturbed orbit of flexible mylar is investigated. However, the source of such flexing, which can include electrostatic charging, is not considered in this prior work. In GEO, the relatively hot plasma environment creates conditions that can charge conducting objects to potentials as high as -30 kV [6]. A crumpled sheet could become stretched out by electrostatic inflation under such conditions, dramatically changing its surface area, while Lorentz forces could decrease the surface area by crumpling a flat sheet. Such dramatic changes in area will significantly perturb the object's orbit by altering the effect of SRP and, in Low Earth Orbits (LEO), the atmospheric drag.

Modeling the motion of a flexible material under electrostatic actuation is challenging due to the complex electrostatic force interactions present. This work seeks to apply the Multi-sphere Method (MSM), a system originally developed for faster-than-realtime approximation of the electric field about a general rigid object, to estimate electrostatic forces and torques between close-proximity Resident Space Objects (RSOs). Thus far, MSM has been based on an assumption of a rigid object with a continuously conducting surface. Here, the fixed shape assumption is relaxed and the MSM methodology applied to simulating the electrostatic deflection of a flexible one dimensional structure in vacuum, which is approximated experimentally by a thin strip of aluminized mylar. The numerical simulation of the deformation is compared to experimental results. The Electrostatic Charging Laboratory for Interactions between Plasma and Spacecraft (ECLIPS) chamber located within the Autonomous Vehicle Systems (AVS) Laboratory at the University of Colorado Boulder (CU Boulder), illustrated in Figure 1, is used to create a high-vacuum environment for the exper-

iments. The unforced strip is used to develop an MSM model, which is then used to simulate the behavior of the strip when an electrostatic charge is added to it and an electric field. The numerical results for the strip deflection are compared to the experimental results to assess the validity of the MSM method for simulating non-rigid bodies.

MSM OVERVIEW

MSM is an accurate, computationally efficient method of approximating the electrostatic interactions between conductors.The general shape is replaced with a series of body-fixed spheres whose radii are chosen such that the resulting electrostatic field closely approximates the true field generated by this shape. Two main categories of MSM exist: Volume MSM (VMSM) and Surface MSM (SMSM).[9] VMSM requires that both sphere radii and placement are optimized to match forces and torques [10], capacitance [11], or electric fields [12]. SMSM, on the other hand, places spheres equidistantly on the surface of the modeled object, and optimizes only the sphere radii to match any of the physical quantities listed above. For the investigation to follow, a SMSM model using capacitance matching is employed. This optimization method is chosen because capacitance matching is more reliable than force and torque matching.

A significant challenge of applying MSM on-orbit is the development of MSM models for poorly-understood objects such as debris. Several solutions to this problem have been proposed. One analyzes orbital perturbations due to Coulomb interactions between a servicer craft whose voltage is known and a debris object to determine the charge distribution on the debris and develop an MSM model.[13] Another uses a dual-Langmuir probe system on board a servicer craft to determine the proper MSM model for a rotating craft or object.[14]

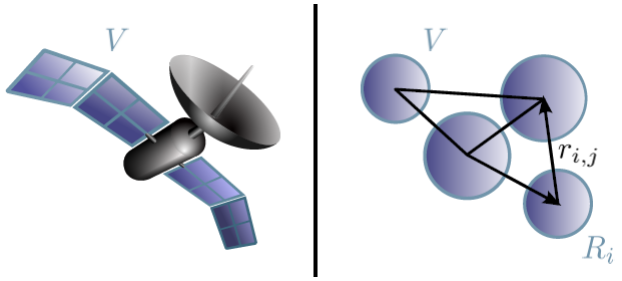

Figure 2. Replacement of complex geometries with MSM spherical shells

Figure 2 depicts the MSM concept. The voltage on each of the spheres shown is related to the charge on that sphere by

$$V_i = k_c \frac{Q_i}{R_i} + k_c \sum_{j=1, j\neq i}^{n} \frac{Q_j}{r_{i,j}} \tag{1}$$

where $k_c = 8.99 \times 10^9$ Nm^2/C^2 is Coulomb's constant, R_j is the radius of the j^{th} sphere, and $r_{i,j}$ is the distance between the i^{th} and j^{th} spheres. These relations can be rewritten into a single matrix equation.

$$\begin{pmatrix} V_1 \\ V_2 \\ \vdots \\ V_n \end{pmatrix} = k_c \begin{bmatrix} 1/R_1 & 1/r_{1,2} & \dots & 1/r_{1,n} \\ 1/r_{2,1} & 1/R_2 & \dots & 2/r_{2,n} \\ \vdots & \vdots & \ddots & \vdots \\ 1/r_{n,1} & 1/r_{n,2} & \dots & 1/R_n \end{bmatrix} \begin{pmatrix} Q_1 \\ Q_2 \\ \vdots \\ Q_n \end{pmatrix}, \quad \mathbf{V} = [S]\mathbf{Q} \tag{2}$$

The matrix $[S]$ is called the elastance matrix. Another, well-known expression relating charge to voltage, $\mathbf{Q} = [C]\mathbf{V}$ indicates that the capacitance is the inverse of the elastance matrix.

$$\mathbf{Q} = [S]^{-1}\mathbf{V} \tag{3}$$

This form is preferable in the electrostatic force and torque evaluation process as the voltage is usually known and the dynamics are dependent on charge. For a single rigid structure, the capacitance matrix is constant. If multiple rigid bodies are modeled then diagonal blocks of the elastance matrix which — when inverted — represent the self-capacitance of each rigid body are constant, while the off-diagonal blocks very with time as the relative positions of these bodies varies.[9, 10, 12] Expansion to consider a flexible structure also requires a time varying elastance matrix. The MSM radii R_j are held constant, but the relative distances $r_{i,j}$ change as the object flexes. In contrast to prior work, even the self-capacitance matrix of such a flexible object will now vary with time.

This paper presents the following hypothesis. To adjust the existing MSM electrostatic force and torque modeling technique to a body with a time varying shape, the body is first decomposed into a finite set of surface segments. The relative degrees of freedom between these surface elements are assumed to be known, i.e. how does one element rotate or hinge relative to another element. Next, either a VMSM or SMSM model is created for each shape element. These spheres are now on fixed locations relative to this element. As the shape changes and the relative position of the surface elements vary with time, the locations of the spheres must be updated at each time step. This creates a time varying elastance matrix that is readily setup using the MSM modeling technique. This modeling approach is justified as Poisson's electrostatic field equation allows for super-position of charge solution. This is how we are able to use MSM to model the electric field between neighboring rigid space objects. Losses in numerical accuracy occur because the MSM model is only an approximation of the true electric field about this shape segment. If two bodies have separation distances that are on the order of the spacecraft dimensions, prior work has shown that these approximations are as good as 1% or less.[12]. To apply this to a flexible shape the segments are essentially docked with a flexible joint. The accuracy is thus determined through both the number of shape segments (i.e. the finite element meshing) and the number of spheres used to represent the electric field of an individual mesh.

To illustrate how this flexible shape MSM is set up, consider Figure 3. For this case, it is assume that the radii of the MSM spheres are all similar, but this is not a necessary condition. The charge-voltage relationship is then setup with the MSM formulation to yield the following elastance matrix.

$$\left[\begin{array}{c} V_1 \\ \hdashline V_2 \\ \hdashline V_3 \end{array}\right] = k_c \left[\begin{array}{c:c:c} 1/R & 1/r_{1,2} & 1/r_{1,3} \\ \hdashline 1/r_{2,1} & 1/R & 1/r_{2,3} \\ \hdashline 1/r_{3,1} & 1/r_{3,1} & 1/R \end{array}\right] \left[\begin{array}{c} Q_1 \\ \hdashline Q_2 \\ \hdashline Q_3 \end{array}\right] \tag{4}$$

The diagonal block elements of the elastance matrix remain constant as the body flexes, while the off-diagonal elements must be updated each time step with the current relative positions of the surface elements.

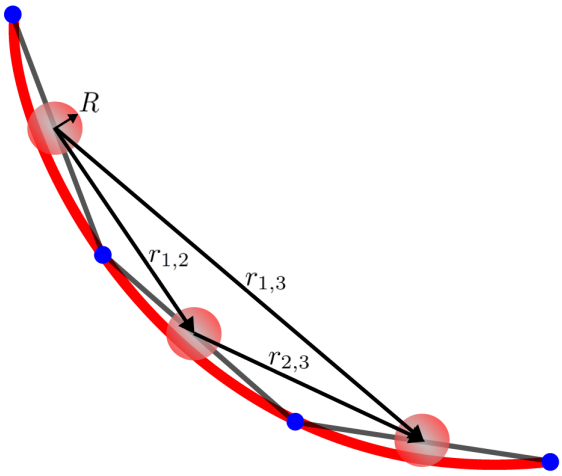

Figure 3. MSM model of multi-link pendulum

COMPARISON TO ANALYTICAL CAPACITANCE SOLUTION

This paper applies this flexible MSM concept to a 1-dimensional, flexible conducting structure. For example, Figure 3 shows how a flexible wire is modeled as a multi-link pendulum with MSM spheres placed at the center of each link. The capacitance of a long, thin, straight wire is given by [15].

$$C = \frac{l}{k_c \Lambda}\left[1 + \frac{1}{\Lambda}(1 - \ln 2) + \frac{1}{\Lambda^2}\left(1 + (1 - \ln 2)^2 - \frac{\pi^2}{12}\right) + \mathcal{O}\left(\frac{1}{\Lambda^3}\right)\right], \quad \Lambda = \ln\left(\frac{l}{a}\right) \tag{5}$$

where l is the length of the wire and a is its radius. This equation is valid for large Λ, which requires that the wire length is much greater than the radius. This scalar value is used to optimize the radius R used in the model. The comparison to the capacitance described in Eq. (3) is accomplished by summing the members of the matrix capacitance as in Eq. (6).

$$C_{\text{scalar}} = \sum_{j=1}^{n}\sum_{i=1}^{n} C_{i,j} \tag{6}$$

If the wire changes shape, Eq. (5) no longer holds. However, the optimization to generate the sphere radii on the diagonal of the elastance matrix is computationally expensive, and determining the nominal capacitance to which to optimize is non-trivial for complicated shapes such as a flexing wire. The error resulting from holding these diagonal components constant while letting the off-diagonal terms in Eq. (4) vary as the shape changes is investigated to determine if re-optimization is strictly necessary.

The case of an anchor ring is considered, as it is another configuration for which there an analytic capacitance has been determined. Reference [16] shows that the capacitance of an anchor ring whose cross sectional radius r is small compared to the ring radius ρ is

$$C = \frac{\pi\rho}{k_c \ln\left(8\rho/r\right)} \tag{7}$$

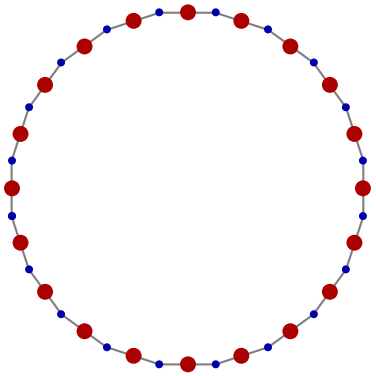

Figure 4. 20-link SMSM model of an anchor ring. The blue circles indicate the hinge locations, while the red accurately represent the SMSM sphere radii optimized using Eq. (5)

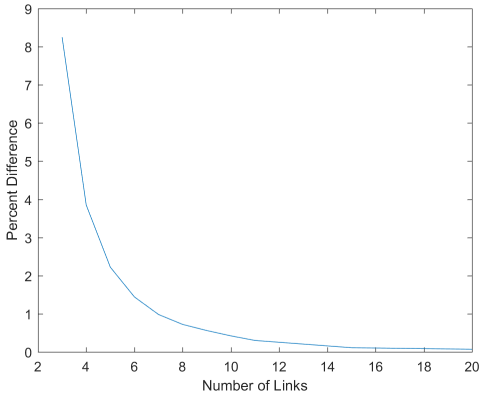

Figure 5. Percent difference between SMSM and analytic anchor ring capacitance for various numbers of links

Two configurations of a 20-link system similar to that shown in Figure 3 are compared. First, the link is arrayed as a straight line and the SMSM sphere radii are optimized to match the capacitance in Eq. (5). The SMSM system is then rearranged into a ring shape without changing the SMSM sphere locations within each link, or the sphere radii to match the capacitance of the ring. The off-diagonal terms of the capacitance matrix account for this new geometry and the sum of all matrix elements is compared to the analytical result in Eq. (7).

The resulting non-optimized SMSM capacitance of the ring calculated using the elastance matrix is within 0.1% of the analytic solution given by Eq. (7) for a 20-link system. A portion of this error is due to the discrete nature of the ring in Figure 4. Figure 5 shows that the difference between the SMSM capacitance and that from Eq. (7) decreases with the number of links, but is still small for low-order systems. Therefore, the capacitance can be well-approximated by an SMSM model without re-optimizing at each time step.

CHARGED WIRE EQUATIONS OF MOTION USING FLEXIBLE MSM

As illustrated in Figures 3 and 6, the flexible, conducting wire studied is approximated as a multi-link pendulum system with SMSM spheres placed at the center of each link. In Figure 6, a single

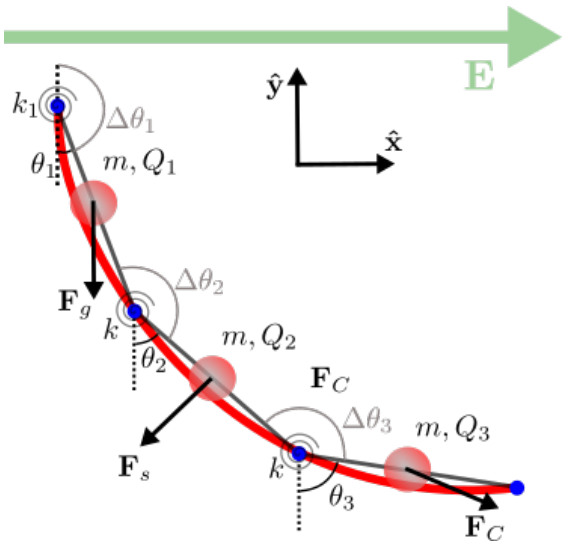

Figure 6. SMSM model of a wire showing forces

force is shown at each sphere position for clarity, but in the model all three forces are applied at all three locations. The sphere position is held at link-center due to the symmetry of the simple shape segments. To account for the stiffness of the wire, torsional springs are simulated at the hinge points of the model. Damping is also applied at these points to account for energy being removed as the modeled wire flexes, though this is not explicitly labeled in Figure 6. The spring constants are the main tunable parameter of the flexible membrane structure, and empirical methods are applied in the next section to provide their nominal values. Note that in Figure 6, the first spring is labeled with a different spring constant, k_1, than the others. This accounts for an attachment mechanism in the model that affects only the first link. Another deviation from the normal material spring constant occurs at the point of the sharp bend introduced in the strip, as seen in Figure 8. This kink introduced near the center of the experimental strip facilitates a significant change in the shape of the strip, providing a more interesting shape to model. A schematic of the model and forces are shown in Figure 6. Note that the directions of the gravitational force $\mathbf{F}_g$ does not change, while the Coulomb and spring forces, $\mathbf{F}_C, \mathbf{F}_\mathrm{s}$ change as the wire deforms. The direction of the Coulomb force changes in time because, in addition to the static electric field in the $\hat{x}$ direction, mutual Coulomb repulsion is applied at each sphere. This is accounted for in the direction of $\mathbf{F}_\mathrm{C}$ in Figure 6.

The gravitational force and spring torque are related to the mass of a link m and the relative angles between two links $\Delta\theta$, respectively.

$$\mathbf{F}_g = mg(-\hat{\mathbf{y}}) \tag{8a}$$

$$\boldsymbol{\tau}_s = k(\Delta\theta - \Delta\theta_0)(-\boldsymbol{\Delta\hat{\theta}}) \tag{8b}$$

Here g is the gravitational acceleration on Earth's surface, k is the spring constant of the torsional spring, $\Delta\theta_0$ is the equilibrium angle between the two links, and $\boldsymbol{\Delta\hat{\theta}}$ is the unit direction vector about which the two shape segments hinge. Assuming a perfectly vertical and constant gravitational field,the potential energy of each link relative to an initial vertical position can be expressed in the well known form

$$U_g = mg(y - y_0) \tag{9}$$

where $(y - y_0)$ is the height of the center of mass above the equilibrium position.The derivation of spring potential energy for the multi-link system is less obvious, but is clearly dependent on the difference in angles between any two links.

$$U_s = \frac{1}{2}k(\Delta\theta - \Delta\theta_0)^2 \tag{10}$$

The $\Delta\theta_0$ term is included in Equation Eq. (10) to account for the shape in Figure 8. As mentioned above, the spring constant k for the first and third hinge point of the model is varied from the other to account for the attachment mechanism and introduced kink, respectively. The kinetic energy of each link consists of two components: translation of the center of mass and rotation of a thin rod about its end.

$$T = \frac{1}{2}m\mathbf{v}_{\text{com}} \cdot \mathbf{v}_{\text{com}} + \frac{1}{2}\boldsymbol{\omega}^T I\boldsymbol{\omega} = \frac{1}{2}mv_{\text{com}}^2 + \frac{1}{6}ml^2\dot{\theta}^2 \tag{11}$$

Above, v_{com} is a link's center of mass velocity, l is the length of a link, and $\dot{\theta}$ is the inertial angular velocity of a link. The Lagrangian of the multi-link pendulum system is therefore

$$\mathcal{L} = T - U = \sum_{i=1}^{n}\left(\frac{1}{2}mv_{\text{com}_i}^2 + \frac{1}{6}ml\dot{\theta}_i^2 - mg(y_i - y_{0_i}) - \frac{1}{2}k_i[\Delta\theta_i - \Delta\theta_{0_i}]^2\right) \tag{12}$$

where n is the number of links. These n, coupled differential equations are numerically solved simultaneously. The dynamics of the system are determined from Lagrange's Equation.

$$\frac{\mathrm{d}}{\mathrm{d}t}\left(\frac{\partial\mathcal{L}}{\partial\dot{q}_i}\right) - \frac{\partial\mathcal{L}}{\partial q_i} = \mathcal{Q}_i \tag{13}$$

Here, q is a generalized coordinate — in this case the inertial angle of a link — and $\mathcal{Q}$ is the sum of generalized, non-conservative forces and torques on a given link. Only two such influences are included in this model: a velocity damping term and the Coulomb force. Velocity damping was chosen for computational efficiency — a significant challenge of this work — and because exercises with the model indicated that neither the type nor rate of damping affected the steady state of the experimental setup. Other damping terms would have been investigated if the transient behavior of the system were the focus of this work. The value of b is a scaling coefficient that determines the settling time of the system. As indicated previously, changing the settling time of the system does not affect the steady-state position of the multi-link system. It is therefore set to a value that brings the modeled wire to its steady-state quickly, as some experiments took several minutes to settle.

The Coulomb force is applied as a generalized force because, generally, the charge on each sphere is allowed to vary. Under this condition, the force is not conservative. Since the capacitance matrix varies as the shape of the wire changes, the Coulomb force is not conservative and therefore must be implemented as a generalized force in the Lagrangian formalism. The forces and torques used to calculate the generalized force on each link are

$$\mathbf{F}_{C_i} = Q_i\left(\mathbf{E} + \sum_{j\neq i}^{n}\frac{Q_j}{(r_i - r_j)^3}(\boldsymbol{r}_i - \boldsymbol{r}_j)\right), \quad \boldsymbol{\tau}_{d_i} = -bv_i^2\hat{\boldsymbol{v}}_i \tag{14}$$

In Eq. (14), Q is the charge on a given sphere and $\boldsymbol{r}$ its position vector; $\mathbf{E}$ is the background electric field; v is the velocity of a given link; and b is a scaling factor for the damping, as described above. For the experiments in this paper a flat, constant electric field is used. Superimposed upon this background electric field is the mutual repulsion of the strip which is included as the second term in the Coulomb force in Eq. (14). In the MSM framework, this is modeled as mutual repulsion between each MSM sphere. Therefore, the Coulomb force experience by each link varies not only as the charge on each strip does, but as the wire deforms and the relative distances between the MSM spheres change.

The equation for the generalized force on the i^{th} sphere is

$$\mathcal{Q}_i = \sum_{j=1}^{n} \mathbf{F}_j \cdot \frac{\partial \mathbf{r}_j}{\partial q_i} \tag{15}$$

where j is a sum over all links within the system, i indicates the relevant equation of motion, and $\mathbf{r}_j$ is the position on the j^{th} link at which the total force $\mathbf{F}_j$ is applied.

Mathematica is used to generate and solve the full equations of motion of the multi-link model. Numerical solutions to the equations of motion are used because, for large numbers of links, the analytical forms are extremely complex. Even without analytic evaluation, only a 5-link system could be used. The `NDSolve` function is given initial conditions derived from the experiments described in the next section and integrates the equations of motion to provide the inertial angles and their corresponding angular velocities at each time step.

EXPERIMENTAL DESIGN & ANALYSIS

Experimental Setup

Validation of the MSM system to flexible structures is achieved through comparison with experiment. A parallel plate capacitor is chosen to produce a flat electric field. This work expands on prior analysis performed in atmosphere, extending those experiments to vacuum. Experiments were conducted within the ECLIPS chamber pictured in Figures 1 and 7a at pressures below 10^{-6} Torr to avoid electrostatic discharge events. The desire for a more space-like environment motivated the vacuum experiments. Air drafts and ionization of ambient air in atmospheric tests complicated previous analyses.[17]

Figure 7a shows the experiment setup. The stand-in for a one-dimensional conducting structure is a thin strip of aluminized mylar, which consists of two coatings of 100 Å thick aluminum on either side of 7 μm mylar substrate. The aluminum coatings, which are normally isolated by the mylar are connected by placing sections of the multi-strand wire from the power supply on both sides of the strip. This strip is suspended mid-way between the cathode and anode of the parallel plate capacitor. This allows the strip to be charged to different potentials than the plates. This mimics the space environment, as environmental currents to RSOs are not necessarily dependent on the local electromagnetic fields.

A Spellman CZE3000 high voltage power supply (HVPS) controlled by LabVIEW via a National Instruments USB data acquisition (DAQ) unit is used to put an excess of charge on the thin strip. The cathode of the parallel plate capacitor is attached to a SL300 HVPS, while the anode is connected to ground. A strip of dimension 7.2 cm $\times$ 0.1 cm was used for all experiments. A kink was introduced at the center of the strip to encourage a significant shape change — a more interesting situation to model than a flat strip merely bending at the attachment point.

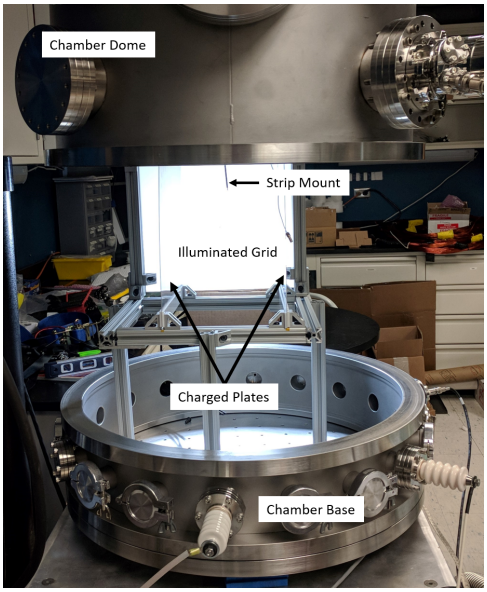

(a) Experimental setup within the ECLIPS chamber

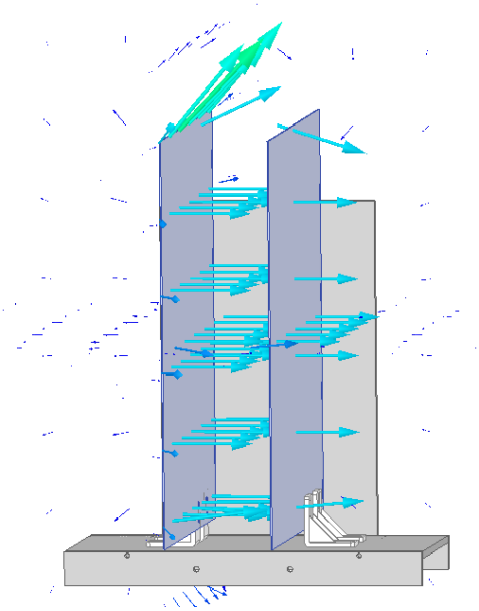

(b) ANSYS Maxwell 3D electric field analysis for experiment structure

Figure 7. Experimental Setup Illustration

The commercial finite element solver Maxwell 3D is used to verify that a flat, constant electric field is generated by the parallel plate capacitor used. Figure 7b shows the electric field of a modified experimental system from that shown in Figure 7a imported into Maxwell 3D with accurate material properties and a voltage drop of $\Delta V = 5$ kV across the plates. This simulation was run at several voltages to determine the electric field for a variety of test voltages. All matched the well-known parallel plate capacitor equation: $E = \frac{\Delta V}{d}$ where d is the plate separation. Note that Figure 7b shows that the electric field between the plates is flat everywhere except near edges. The aluminized mylar strip was therefore positioned near the middle of the setup, far from any edges in all experiments.

Experiment Analysis

To analyze the experiment as various voltages were applied to both the strip and the cathode of the parallel plate capacitor depicted in Figure 7a, images were taken and loaded in MATLAB for each trial. Edge finding algorithms in MATLAB Image Processing toolbox were used to differentiate the wire from its surroundings. A grid of holes was drilled into a sheet of Delrin using a CNC machine and placed behind the wire to identify the conversion factor from pixels to inches. The orientation of the grid points in the Delrin sheet provided an arbitrary vertical axis to which the image can be aligned eliminating the need to align the camera itself. Furthermore, the grid points allowed for a comprehensive total alignment and warp analysis on the background Delrin sheet.

After isolating the strip edges as seen in Figure 8, the positions of the edges were averaged at each y-value to find the centerline. The resultant centerline data was smoothed to reduce high frequency noise prior to curve fitting using a Gaussian-weighted moving average filter. The data was then divided into two segments, split by the kink that had been introduced near the middle of the mylar

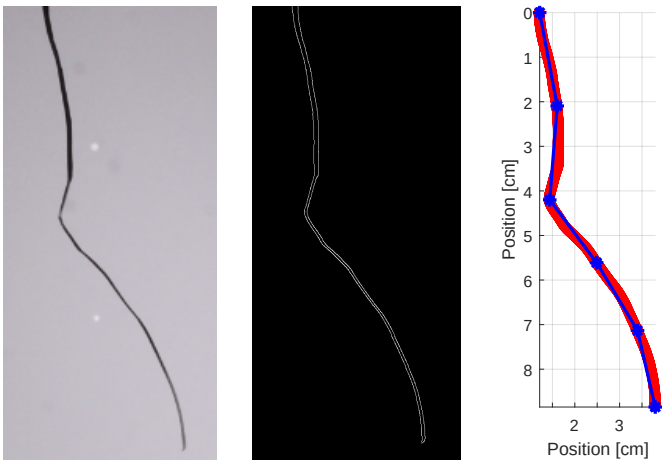

(a) Initial strip image (b) Edge finding result (c) 5 link system extracted from data

Figure 8. Image analysis results

strip. A piecewise cubit Hermite interpolating polynomial was then fit to the smoothed data on each side of the strip.

Once the interpolating function is obtained, it is used to develop a discrete, n-link system for comparison with the n-link model; here, $n = 5$, however this could be expanded to higher order systems in future work. The positions of the hinges found based on the curve fit were compared to steady state hinge positions for accuracy as shown in Figure 8. Moreover, the inertial and relative angles for each link in the n-link system are calculated to initialize the model and solve the equations of motion for the strip.

An analysis is performed on the grid points to quantify any camera misalignment and warp in the Delrin sheet in the background. Grid positions are found by calculating the center of mass of each grid point using the MATLAB's `regionprops` built-in function as they are shown in Figure 9. Once obtained, the distances between the grid points are used to derive the conversion factor from pixels to inches which was calculated to approximately 150 $^{\text{pixels}}/_{\text{cm}}$.

Finally, the standard deviation of the grid using the separation distances of the its intersections is calculated as the means to quantify any camera misalignment or warp in the Delrin sheet. The standard deviation came out to be 1.92 pixels which is significantly less than the pixel to cm conversion factor. This implies that the camera misalignment and warp in the Delrin sheet were negligible.

RESULTS & DISCUSSION

Table 1 shows the voltage levels for each experiment conducted. The plate voltage is applied to the cathode of the parallel plate capacitor while the anode is set to ground. Numerical simulations are compared to experimental data in Figure 10. Three separate spring constants are used to account for the attachment mechanism, kink, and the nominal portions of the strip. These values are tuned within the model to match the initial, unforced shape and position of the object to a Test 1. The spring forces determined from this exercise are used to initialize the model to an additional three experiments, each with different voltage parameters.

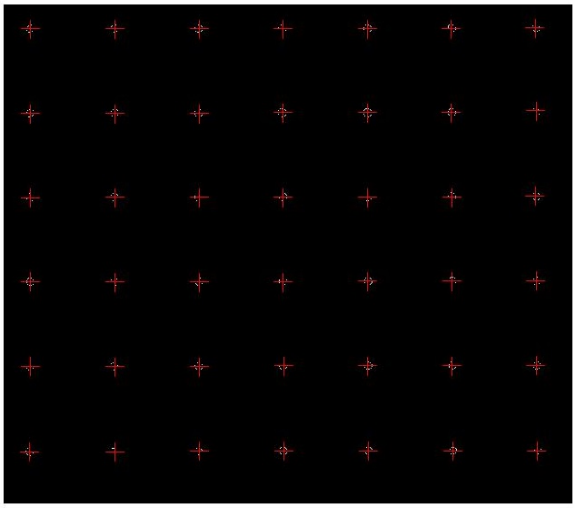

Figure 9. Centers of the CNC grided points on the Delrin sheet detected using the Image Processing toolbox in MATLAB

Figure 11 provides a quantitative indication of the position error between the hinge points in the model and those found from the experiment as shown in Figure 8.

It is clear from the figure that as the voltage gets farther from that in Test 1, the model match begins to degrade. Note however that the shape of the wire seems still to match that of the experiment. The SMSM model is developed to match Test 1, so having a good fit there is expected. When this same behavior was seen in previous atmospheric experiments, it was postulated that large strip voltages were ionizing the air, creating plasma that would then shield the strip from the background electric field. While this effect can't be ruled out completely as an actor in previous experiments, all experiments shown in Figure 10 were performed in vacuum, precluding this effect.

Table 1. System voltages for experiments

Test #	Plate Voltages (V)	Strip Voltages (V)
1	2000	6000
2	2000	5000
3	1000	3000
4	1000	1000

Two effects, illustrated in Figure 12, were observed and investigated which could be the cause of the modeling errors seen in Figures 10 and 11. Figure 12a shows that, under seemingly identical charging conditions, the strip feels different forces and torques. The yellow, right-most line represents the position of strip with V_{plate} = 1 kV and V_{strip} = 0 kV before the strip was charged. The lines to the left are its position under the same voltage settings after experiments in which the strip was charged to progressively higher voltages. This seems to indicate that the mylar, which is an insulator and therefore does not charge and discharge on the fast timescales upon which conductors do, was accumulating charge as consecutive experiments were performed. As the model did not account for this dielectric charging effect, it is unsurprising that Tests 2-4 deviate from experiments.

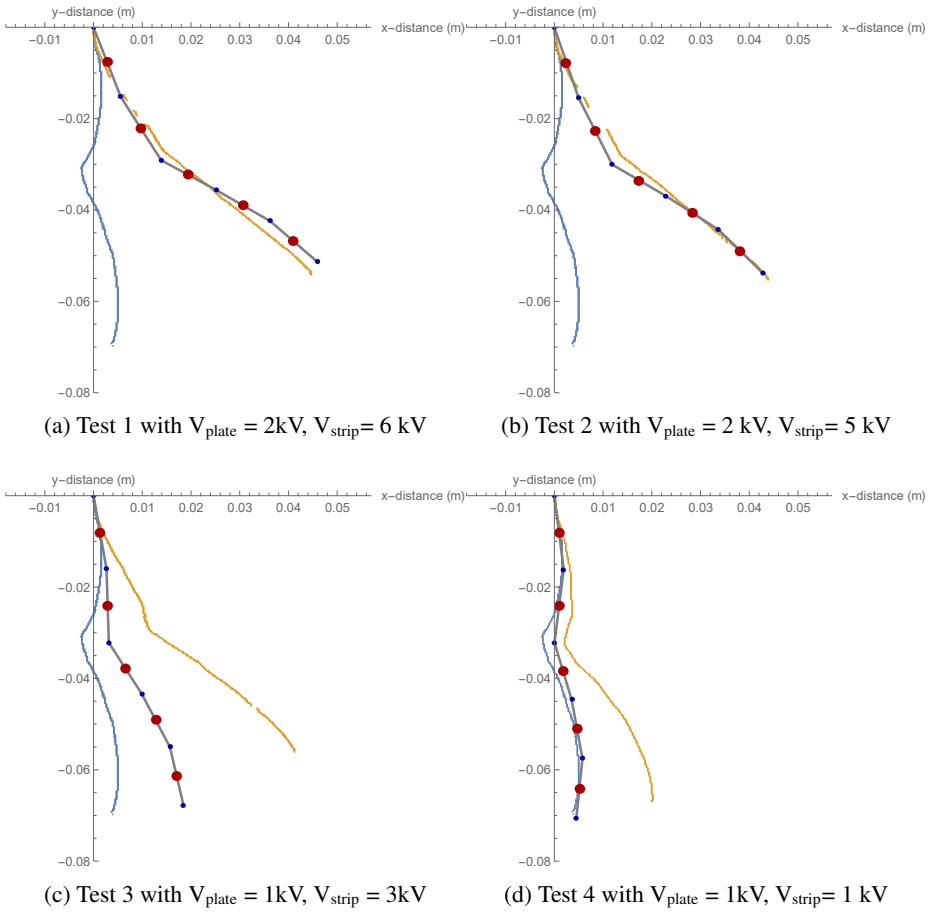

(a) Test 1 with V_{plate} = 2kV, V_{strip}= 6 kV

(b) Test 2 with V_{plate} = 2 kV, V_{strip}= 5 kV

(c) Test 3 with V_{plate} = 1kV, V_{strip} = 3kV

(d) Test 4 with V_{plate} = 1kV, V_{strip}= 1 kV

Figure 10. Results of numerical simulations. The blue line represents initial, unforced wire shape while the yellow line represents steady-state experimental configuration. The gray line is the steady-state position calculated using the model described above. On this line, the red spheres represent the placement of the SMSM spheres as well as their actual radii, while the smaller, blue dots represent the hinges between each of the pendulums.

The second effect not accounted for in the model is the mutual capacitance of the strip and the plate. To illustrate how this occurs, consider the inverse of Eq. (4), but for three electrically isolated spheres each charged by separate power supplies.

$$\begin{bmatrix} Q_1 \\ Q_2 \\ Q_3 \end{bmatrix} = \begin{bmatrix} C_{1,1} & C_{1,2} & C_{1,3} \\ C_{2,1} & C_{2,2} & C_{2,3} \\ C_{3,1} & C_{3,1} & C_{3,3} \end{bmatrix} \begin{bmatrix} V_1 \\ V_2 \\ V_3 \end{bmatrix} \tag{16}$$

It is immediately clear that even though there is no current flow between spheres, the charge Q_1 is dictated not only by its own voltage and capacitance but also by the proximity to the other two charged spheres.

$$Q_1 = C_{1,1}V_1 + C_{1,2}V_2 + C_{1,3}V_3 \tag{17}$$

While stray electric fields can be generated in the space environment due to plasma interactions, these are less common on Earth. Thus, this mutual capacitance effect can be mitigated, but not

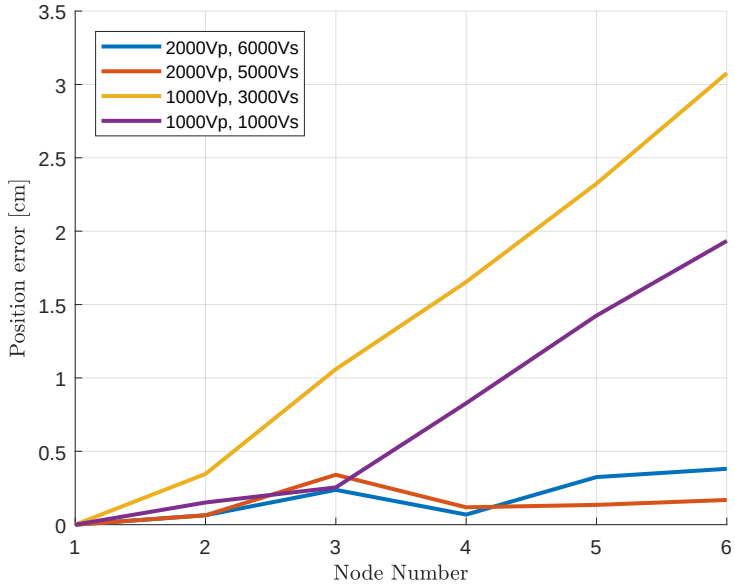

Figure 11. Position difference between hinge positions between the model and experimental data for Tests 1-4

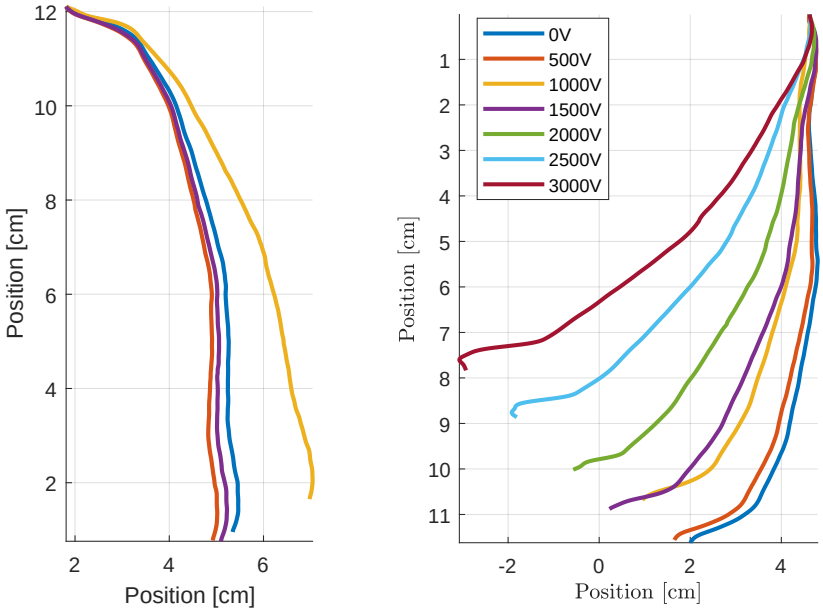

(a) Position of experimental strip with V_{plate}= 1 kV, V_{strip} = 0 kV. The drift from the original test (yellow) to the left originated after successive charge cycles.

(b) Position of experimental strip with V_{plate} increased from 0 kV (far right) to 3 kV (far left) and V_{strip} = 0 kV.

Figure 12. Indication of unmodeled physical phenomena of dielectric charging of the aluminized mylar strip as well as induced charging effects with the parallel plate capacitor generating the background electric field

avoided in terrestrial experiments. Note in Eq. (17) that, if V_1 and V_2 are sufficiently small, $Q_1 \approx C_{1,1}V_1$.

For the case with the parallel plate capacitors, the plates are extremely large compared with the strip, meaning that the mutual capacitance is also large. This is why the majority of the experiments outlined in Table 1 have $V_{\text{strip}} > V_{\text{plate}}$. Note that Test 4 is fit most poorly by the model. This is in part because the charging due to mutual capacitance is large for that case.

Figure 12b shows deflection of the strip when grounded for various plate voltages. As the mutual capacitance between the strip and the plate is unknown and changes in time, this effect can't be incorporated into the model. Additionally, extremely low plate voltages necessitate excessive strip voltages to achieve significant shape change. This circumstance exacerbates the dielectric charging issue discussed previously. However the relative success of Tests 2 and 3 indicate that an object like aluminized mylar can be modeled with relative accuracy in certain circumstances.

CONCLUSIONS

The paper presents a hypothesis on how to model flexible shapes using an augmented Multi-Sphere-Method (MSM). The time varying shape is discretized into finite segments, and MSM models are developed for each. This approach is suitable for large shape changes as illustrated through analytical matching with a line deforming to a circle. A key interest for charged deformable shapes are torn of mylar sheets. To see how well this technique would work to model such challenging thin structures, experiments on flexible conductors are compared to numerical simulations using MSM. All experiments and simulations were conducted using a flat, constant electric field under vacuum. Steady state behaviors of a flexible, nearly 1-dimensional strip of aluminized mylar are investigated for various charge levels and background electric field. Results indicate that charging of the insulating mylar plays a significant role in the dynamics. Modeling only the charge on the conductor provides a baseline for shape change and deflection, but is not sufficient to fully predict how such an object would behave in the space environment.

ACKNOWLEDGMENT

This work was supported by Air Force Office of Scientific Research (AFOSR) Grant FA9550-15-1-0407.

REFERENCES

[1] John H. Cover, Wolfgang Knauer, and Hans A. Maurer. Lightweigth reflecting structures using electrostatic inflation, 1966.

[2] Laura A. Stiles, Hanspeter Schaub, Kurt Maute, and Daniel F. Moorer. Electrostatic inflation of membrane space structures. In *AAS/AIAA Astrodynamics Specialist Conference*, Toronto, Canada, Aug. 2–5 2010. Paper No. AIAA-2010–8134.

[3] Laura A. Stiles, Hanspeter Schaub, Kurt K. Maute, and Daniel F. Moorer. Electrostatically inflated gossamer space structure voltage requirements due to orbital perturbations. *Acta Astronautica*, 84:109–121, Mar.–Apr. 2013.

[4] Smriti Nandan Paul and Carolin Frueh. Space Debris Charging and its Effect on Orbit Evolution. In *AIAA/AAS Astrodynamics Specialist Conference*, pages 1–31, Long Beach, CA, 2009.

[5] Joseph Hughes and Hanspeter Schaub. Rapid charged geosynchronous debris perturbation modeling of electromagnetic disturbances. In *AAS Spaceflight Mechanics Meeting*, San Antonio, TX, Feb. 5–9 2017. Paper AAS 17–320.

[6] Carolin Früh, Dale Ferguson, Chin Lin, and Moriba Jah. The effect of passive electrostatic charging on near-geosyncronous high area-to-mass ratio objets. In *International Astronautical Congress*, volume 64, 2013.

[7] Joseph Hughes and Hanspeter Schaub. Space weather influence on electromagnetic geosynchronous debris perturbations using statistical fluxes. *Space Weather*, 16(4):391–405, 2018.

[8] Sittiporn Channumsin, Matteo Ceriotti, Carolin Früh, and Gianmarco Radice. Orbital dynamics of lightweight flexible debris. In *64th International Astronautical Congress*, Sept. 23–27 2013. Paper No. IAC-13-A6.2.7.

[9] Daan Stevenson and Hanspeter Schaub. Optimization of sphere population for electrostatic multi sphere model. *IEEE Transactions on Plasma Science*, 41(12):3526–3535, Dec. 2013.

[10] Daan Stevenson and Hanspeter Schaub. Multi-sphere method for modeling electrostatic forces and torques. *Advances in Space Research*, 51(1):10–20, Jan. 2013.

[11] Philip Chow, Joseph Hughes, Trevor Bennett, and Hanspeter Schaub. Automated sphere geometry optimization for the volume multi-sphere method. In *AAS/AIAA Spaceflight Mechanics Meeting*, Napa Valley, California, Feb. 14–18 2016. Paper No. AAS-16-472.

[12] Gabriel Ingram, Joseph Hughes, Trevor Bennett, Christine Hartzell, and Hanspeter Schaub. Autonomous volume multi-sphere-model development using electric field matching. In *AAS Spaceflight Mechanics Meeting*, San Antonio, TX, Feb. 5–9 2017. Paper AAS 17-451.

[13] Trevor Bennett and Hanspeter Schaub. Electrostatically charged spacecraft formation estimation using linearized relative orbit elements. In *AAS Spaceflight Mechanics Meeting*, San Antonio, TX, Feb. 5–9 2017. Paper AAS 17–483.

[14] Heiko Engwerda, Joseph Hughes, and Hanspeter Schaub. Remote sensing for planar electrostatic characterization using the multi-sphere method. In *Final Stardust Conference*, ESTEC, Nederland, Oct. 31 – Nov. 4 2016.

[15] J. D. Jackson. Charge density on thin straight wire , revisited Charge density on thin straight wire , revisited. *American Journal of Physics*, 789(68), 2000.

[16] T.S.E Thomas. The Capacitance of an Anchor Ring. *Australian Journal of Physics*, 7:347, 1954.

[17] Jordan Maxwell and Hanspeter Schaub. Applicability of the multi-sphere method to flexible one-dimensional conducting structures. In *AAS/AIAA Astrodynamics Specialist Conference*, Stevenson, Washington, August 20–24 2017. Paper No. AAS 17-618.